Mechanical Systems and Signal Processing 200 (2023) 110525

Contents lists available at ScienceDirect

Mechanical Systems and Signal Processing

journal homepage: www.elsevier.com/locate/ymssp

Motion magnification-based nonlinear ultrasonic signal enhancement and its application to remaining fatigue life estimation of a steel padeye

Peipei Liu [a,b], Zhanxiong Ma [c], Jinho Jang [c], Hoon Sohn [c,d,*]

[a] School of Civil Engineering, Southeast University, Nanjing 210096, China
[b] China-Pakistan Belt and Road Joint Laboratory on Smart Disaster Prevention of Major Infrastructures, Southeast University, Nanjing 210096, China
[c] Department of Civil and Environmental Engineering, Korea Advanced Institute of Science and Technology, Daejeon 34141, Republic of Korea
[d] Center for 3D Printing Nondestructive Testing, Korea Advanced Institute of Science and Technology, Daejeon 34141, Republic of Korea

ARTICLE INFO

Communicated by Javad Baqersad

Keywords:
Nonlinear ultrasonic modulation
Phase-based motion magnification
Steel padeye
Fatigue crack
Remaining fatigue life estimation

ABSTRACT

In this study, a nonlinear ultrasonic signal enhancement method based on phase-based motion magnification was proposed. First, a two-dimensional (2D) video was constructed from a one-dimensional time-domain ultrasonic signal with an automatically selected pixel scale. The constructed 2D video was spatially decomposed into multiple sub-bands with different spatial scales. The subtle motions of the nonlinear responses of interest were enhanced by phase denoising and magnification in each sub-band. Then, the magnified 2D video was reconstructed by collapsing all the amplified sub-bands. Finally, a magnified ultrasonic signal was extracted from the magnified 2D video for further nonlinear ultrasonic analysis. The proposed method was validated with a group of synthetic signals at different noise levels, and applied in the estimation of the remaining fatigue life of a steel padeye with improved accuracy.

1. Introduction

Nonlinear ultrasonics indicate ultrasonic waves whose frequencies are different from the excitation frequencies and amplitudes that are highly dependent on the crystalline structure of a material as well as on the existence of defects [1]. Incipient defects (e.g., micro fatigue cracks) have been shown to be sources of high nonlinearity [2]. Nonlinear ultrasonics can significantly enhance the sensitivity to interactions with micro defects compared with classical linear ultrasonic features. More specifically, nonlinear ultrasonics manifest through the creation of accompanying harmonics/subharmonics, modulation between different input frequencies, and shifting of resonance frequencies as a function of the input energy [3,4].

In nonlinear ultrasonic modulation, inputs consisting of low- and high-frequency components are normally applied to the target structure through surface-mounted piezoelectric transducers (PZTs) or phased arrays [5], noncontact air-coupled transducers [6], and temporally or spatially modulated lasers [7,8]. Nonlinear modulation components appearing at the sum and difference of input frequencies can be used for fatigue crack detection and localization in metals and concrete [9,10], delamination or weak bond detection

* Corresponding author at: Department of Civil and Environmental Engineering, Korea Advanced Institute of Science and Technology, Daejeon 34141, Republic of Korea.
E-mail address: hoonsohn@kaist.ac.kr (H. Sohn).

https://doi.org/10.1016/j.ymssp.2023.110525
Received 26 January 2023; Received in revised form 15 May 2023; Accepted 10 June 2023
Available online 21 June 2023

in composites [5,11], and porosity evaluation and microstructure characterization in additively manufactured metallic objects [12,13].

A technical obstacle to nonlinear ultrasonic modulation is the difficulty in measuring and analyzing the subtle modulation components, especially in noisy environments. Several attempts have been made to enhance the reliability of defect detection using nonlinear ultrasonic modulation. In one method, the input frequencies were swept to find the optimal frequency combination that amplifies the defect-induced modulation, given that the modulation intensity is dependent on the input frequencies and is likely to be affected by defect configurations [14,15]. However, sweeping the input frequencies is a time-consuming process, which could hinder its field applications. An alternative solution utilized a chirp or pulse signal as the input, but its broadband response increased the complexity of defect characterization [16,17]. Another method denoised the ultrasonic measurement by filtering a spatial signal network acquired by laser scanning [18,19]. However, this method is also restrained by the long data collection time for laser scanning and the high cost of laser ultrasonics.

On the other hand, methods have been developed to capture the nonlinear responses from individual ultrasonic measurements with advanced signal processing. Nonzero bispectrum or trispectrum peaks due to defect-induced harmonics and modulations have been numerically and experimentally demonstrated under noise interference [20,21]. The spectral correlation between nonlinear modulation components was investigated to enhance the nonlinear responses by suppressing noise in the spectral correlation domain [22,23]. In addition, the sequential patterns of nonlinear ultrasonic responses can be determined via artificial neural networks, and distinguished from ultrasonic signals measured in noisy environments [24,25]. The efficacy of capturing nonlinear responses, however, is limited because these methods focused solely on noise suppression.

In this study, we propose a nonlinear ultrasonic signal enhancement method inspired by phase-based motion magnification, which simultaneously enhances the nonlinear modulations and suppresses noise. The proposed method was applied to estimate the remaining fatigue life (RFL) of a steel padeye. The uniqueness of the proposed method is summarized as follows. (1) Ultrasonic signals are converted into a two-dimensional (2D) video with automated parameter selection. (2) Subtle nonlinear ultrasonic responses are amplified by phase manipulation and magnification of the converted 2D video. (3) Time-domain noise can be effectively suppressed by spatial-phase denoising of the converted video. (4) The proposed method can be applied to accurately estimate the RFL.

The remainder of this paper is organized as follows. Section 2 introduces the theoretical basis of nonlinear ultrasonic modulation and phase-based motion magnification. Section 3 describes the proposed motion magnification-based nonlinear ultrasonic signal enhancement method. Section 4 presents the validation of the proposed method with synthetic ultrasonic signals. Section 5 discusses its application in the RFL estimation for a steel padeye. Section 6 concludes with a summary of the study, its limitations, and future work.

2. Theoretical background

2.1. Nonlinear ultrasonic modulation

Nonlinear ultrasonic modulation is a widely used technique based on two distinctive inputs (f_a and f_b, $f_a < f_b$). When a structure exhibits linear behavior, the structural response includes spectral components that correspond only to the inputs. However, when a structure exhibits nonlinear behavior (e.g., owing to material nonlinearity or defects), its response includes components not only at the input frequencies but also their modulation (or sideband) manifestation at $f_b \pm f_a$. For simplicity, the harmonics and higher-order modulations were excluded. For example, nonlinear ultrasonic modulation can occur owing to an asymmetry in the tensile/compression behavior caused by crack opening and closing, as shown in Fig. 1. Correspondingly, a quantitative nonlinear modulation parameter β is expressed as [17]

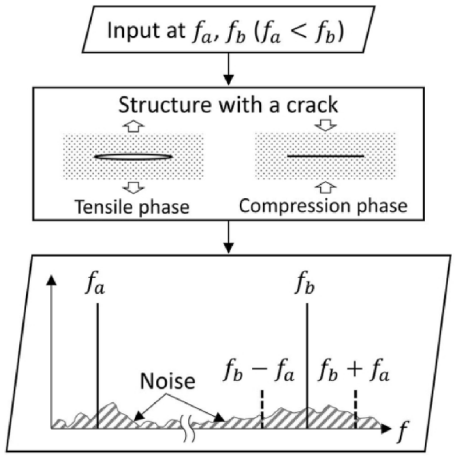

Fig. 1. Illustration of nonlinear ultrasonic modulation.

$$\beta \approx \frac{4(P_s(f_b - f_a) + P_s(f_b + f_a))}{P_s(f_a)P_s(f_b)\kappa_a\kappa_b} \propto \frac{P_s(f_b - f_a) + P_s(f_b + f_a)}{P_s(f_a)P_s(f_b)} \tag{1}$$

where $P_s(f_a)$, $P_s(f_b)$, $P_s(f_b - f_a)$, and $P_s(f_b + f_a)$ are the amplitudes of the structural response at the input and modulation frequencies; and κ_a and κ_b are the wavenumbers corresponding to f_a and f_b, respectively.

β is sensitive to micro defects such as fatigue cracks at their very early stage [5,6]. However, one technical issue is that $P_s(f_b \pm f_a)$ is often at least one or two orders of magnitude smaller than $P_s(f_a)$ and $P_s(f_b)$. It is difficult to precisely extract $P_s(f_b \pm f_a)$ in noisy environments, particularly when the noise overlaps the nonlinear components in the frequency domain (Fig. 1). Although various denoising methods have been developed as mentioned in the previous section, the transition of nonlinear ultrasonic modulation techniques to real field applications remains a challenge.

2.2. Phase-based motion magnification

Motion magnification is used to amplify the unperceivable changes in a video. It can be divided into Lagrangian and Eulerian approaches. Lagrangian approaches extract motions explicitly by tracking the particle trajectories in video frames. However, they are computationally intensive and could introduce errors in the amplified motions [26]. In contrast, Eulerian approaches process the video separately in space and time without direct particle tracking to significantly reduce computational costs [27]. As shown in Fig. 2, Eulerian approaches first spatially decompose a video into an alternative representation, e.g., different spatial sub-bands by Gaussian, Laplacian, or steerable pyramids. Pyramid decomposition provides a flexible and convenient multiresolution format for further image processing. Advanced decomposition can also be achieved by learning from existing examples [28]. Then, a designed temporal filter is applied to the time series of each pixel in the sub-bands to extract the frequency components of interest. The filtered sub-bands are amplified by a magnification factor and then collapsed to reconstruct the output video.

Phase-based motion magnification is based on complex steerable pyramid decomposition. Complex steerable pyramids decompose each video frame into multiple sub-bands according to the spatial scale and orientation; their basis functions resemble Gabor wavelets. Here, the spatial sub-bands are decomposed as [27]

$$\tilde{S}_{\omega,\theta}(k_x, k_y, t) = \tilde{I}(k_x, k_y, t)\Psi_{\omega,\theta}(k_x, k_y) \tag{2}$$

where $\tilde{S}_{\omega,\theta}(k_x, k_y, t)$ is the spatial discrete Fourier transform (DFT) of the decomposed sub-bands $S_{\omega,\theta}(x,y,t)$; $\tilde{I}(k_x, k_y, t)$ is the spatial DFT of each frame in video $I(x,y,t)$; and $\Psi_{\omega,\theta}(k_x, k_y)$ is the frequency-domain transfer function of the complex steerable pyramids scaled and rotated with the spatial scale ω and orientation θ.

The decomposed $S_{\omega,\theta}(x,y,t)$ provides access to the local amplitude and phase in each video frame. The subtle motions can be enhanced by temporal filtering and amplification of the phase variation in $S_{\omega,\theta}(x,y,t)$, resulting in $S'_{\omega,\theta}(x,y,t)$. The amplified sub-bands $S'_{\omega,\theta}(x,y,t)$ are then collapsed over all the scales and orientations as

$$\tilde{I}'(k_x, k_y, t) = \sum \tilde{S}'_{\omega,\theta}(k_x, k_y, t)\Psi_{\omega,\theta}(k_x, k_y) \tag{3}$$

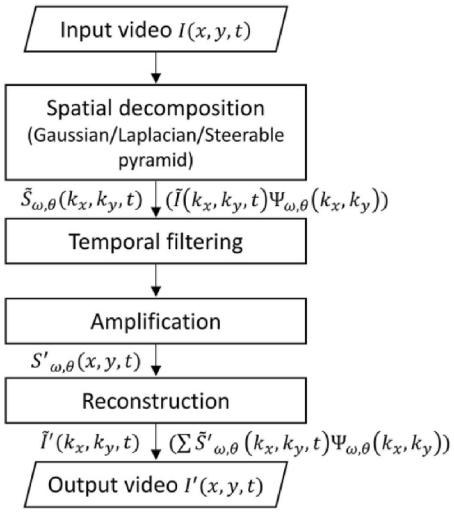

Fig. 2. Generalized framework of Eulerian motion magnification. (Equations are listed for phase-based motion magnification using complex steerable pyramid decomposition.).

where $\tilde{S}'_{\omega,\theta}(k_x,k_y,t)$ is the spatial DFT of $S'_{\omega,\theta}(x,y,t)$. The output video $I'(x,y,t)$ can be obtained by the inverse spatial DFT of $\tilde{I}'(k_x,k_y,t)$.

Compared with other Eulerian motion magnification approaches, phase-based motion magnification enables larger magnifications and improved noise handling [27,29]. It has been widely applied for vision-based mode shape characterization and defect detection [30–32]. In this study, phase-based motion magnification is adopted to enhance the performance of nonlinear ultrasonic analysis.

3. Motion magnification-based nonlinear ultrasonic analysis

Fig. 3 presents a flowchart of the proposed motion magnification-based nonlinear ultrasonic signal enhancement method. For a structure excited at two distinct frequencies (f_a and f_b), its one-dimensional (1D) time-domain response s consists of the linear response s_l (f_a, f_b), nonlinear response s_m ($f_b \pm f_a$, if the structure behaves nonlinearly), and noise s_n. The large motion of the primary linear response s_l can be separated by the bandpass filtering of s to obtain the small-motion signal s_s.

$$s_s = s - s_l = s_m + s_n \tag{4}$$

where s_s contains the nonlinear response s_m and noise s_n.

The small-motion signal is then amplified by the following three steps:

Step 1: Conversion of 1D time-domain signal to a 2D video.

To construct a 2D video $I(x,y,t)$, s_s is segmented, and each segment is used to individually establish the pixel movement in the video. As illustrated in Fig. 4, s_s is divided into N segments, with each segment containing M data points. Here, M is selected to include the integer periods of $f_b \pm f_a$. Each segment is converted into the pixel movement along a designated orientation x and at a fixed y-position as

$$I\left(\frac{s_s((j-1)M+i)}{max|s_s|} \bullet \Delta p, j+1, i \bullet \Delta t\right) = 1 \qquad 0 < i \le M,\ 0 < j \le N \tag{5}$$

where Δt is the time step between two successive data points, and Δp is the pixel scale used to convert the normalized s_s into pixel movement. Δp indicates the largest pixel movement in the constructed video. Note that Δp is automatically determined by considering the noise levels for each ultrasonic measurement s, which will be explained later. $I(x,y,t) = 0$ is assigned for the other pixels. The size of the constructed video is set to $(N+2, N+2, M)$ in this study.

Step 2: Phase-based motion magnification of the constructed 2D video.

Phase-based motion magnification is applied to the constructed 2D video $I(x,y,t)$ for nonlinear ultrasonic signal enhancement, as shown in Fig. 5. The video is decomposed into multiple spatial sub-bands $S_{\omega,\theta}(x,y,t)$ with octave-bandwidth complex steerable pyramids (Eq. (2)). Because the small-motion signal s_s is converted into the pixel movement along the x-orientation, only the sub-bands $S_{\omega,0}(x,y,t)$ ($\theta = 0$) are processed to enhance the nonlinear response. $S_{\omega,0}(x,y,t)$ decomposed at various spatial scales ω can accurately capture the subtle motions, i.e., the nonlinear response s_m, from $I(x,y,t)$.

For an intuitive demonstration, $S_{\omega,0}(x,y,t)$ at a specific spatial scale ω is simplified into a 1D profile $S_{\omega,0}(x,t)$ under global

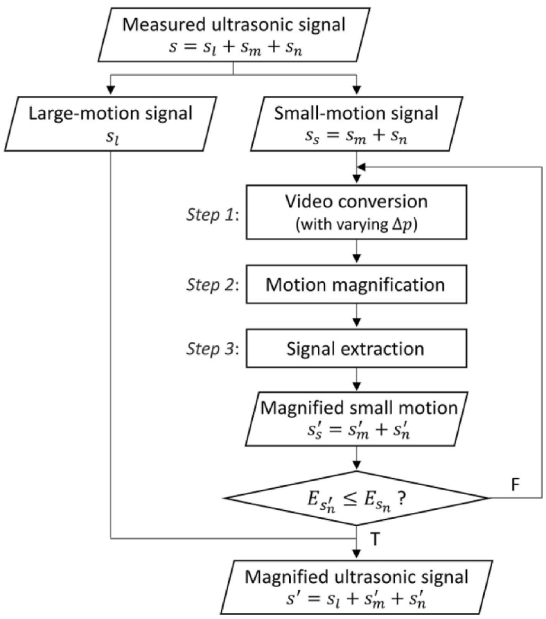

Fig. 3. Flowchart of the motion magnification-based nonlinear ultrasonic signal enhancement method.

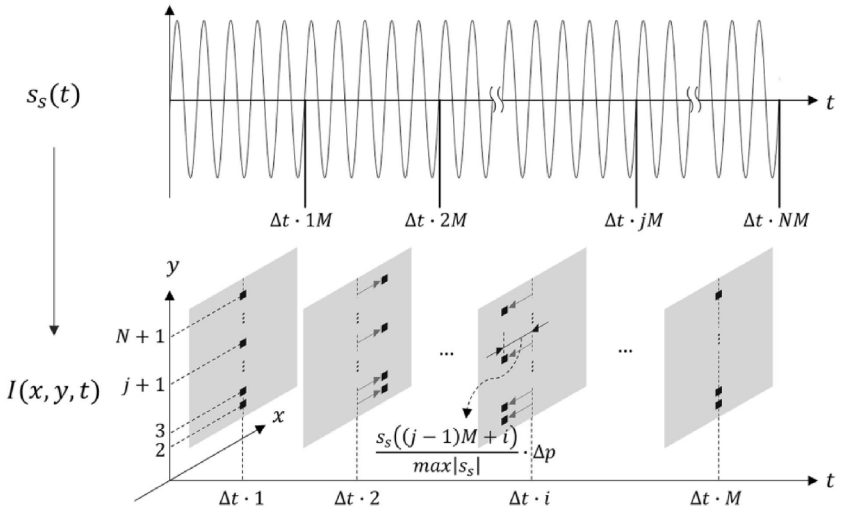

Fig. 4. Video construction using the decomposed small-motion signal s_s.

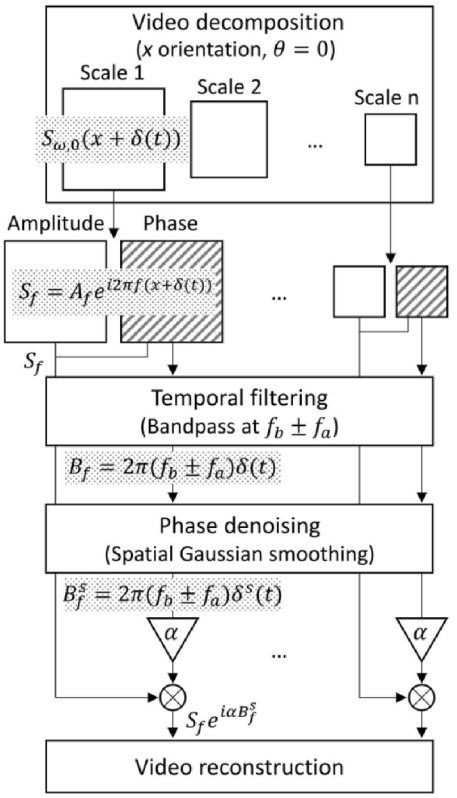

Fig. 5. Phase-based motion magnification for nonlinear signal enhancement.

translation $\delta(t)$ over time ($S_{\omega,0}(x,t) = S_{\omega,0}(x+\delta(t))$). $S_{\omega,0}(x,t)$ can be rewritten as the sum of the complex sinusoids by Fourier series decomposition.

$$S_{\omega,0}(x,t) = \sum_{f=-\infty}^{+\infty} S_f(x,t) = \sum_{f=-\infty}^{+\infty} A_f e^{i2\pi f(x+\delta(t))} \tag{6}$$

where $S_f(x,t) = A_f e^{i2\pi f(x+\delta(t))}$ denotes the component at the temporal frequency f with the amplitude and phase of A_f and $2\pi f(x+\delta(t))$,

respectively. Because the phase contains motion information $\delta(t)$, it can be altered to manipulate motion as in the Fourier shift theorem. To enhance the nonlinear response at $f_b \pm f_a$, we isolate the phase by temporal filtering.

$$B_f(x,t) = 2\pi(f_b \pm f_a)\delta(t) \tag{7}$$

where $B_f(x,t)$ is the isolated phase at $f_b \pm f_a$.

The noise s_n can alter $\delta(t)$ and cause the phase signal $2\pi f(x+\delta(t))$ to become noisy. The direct amplification of the phase signal could amplify the noise in the output video. In this study, because the time length of each segment of s_s equals to integer periods of the nonlinear modulation components at $f_b \pm f_a$, the phase caused by the nonlinear response s_m remains identical among the different pixels, and the phase variations are caused only by the noise s_n. Therefore, phase denoising can be performed by low-passing $B_f(x,t)$ spatially, e.g., by amplitude-weighted spatial Gaussian smoothing of each video frame.

$$B_f^s(x,t) = \frac{(B_f(x,t)A_f)^* \mathrm{K}_\rho(x)}{A_f{}^* \mathrm{K}_\rho(x)} = 2\pi(f_b \pm f_a)\delta^s(t) \tag{8}$$

where $\mathrm{K}_\rho(x)$ is the Gaussian kernel provided by $e^{-\frac{x^2}{\rho^2}}$, ρ is set as equal to the spatial domain filter width ($\rho = N+2$ in this study) to maximize the smoothing effect, and $\delta^s(t)$ is the denoised translation.

The spatially filtered phase $B_f^s(x,t)$ is then multiplied by the magnification factor α, and added to the phase of $S_f(x,t)$ to obtain the motion-magnified $S_f^{'}(x,t)$.

$$S_f^{'}(x,t) = \begin{cases} S_f(x,t)e^{i\alpha B_f^s(x,t)} \\ S_f(x,t) \end{cases} = \begin{cases} A_f e^{i2\pi f(x+\delta(t)+\alpha\delta^s(t))} & f = f_b \pm f_a \\ A_f e^{i2\pi f(x+\delta(t))} & f \neq f_b \pm f_a \end{cases} \tag{9}$$

where the $S_f^{'}(x,t)$ at $f_b \pm f_a$ becomes $S_f(x+(1+\alpha)\delta(t))$ if $\delta^s(t) \approx \delta(t)$. In this case, the motion at $f_b \pm f_a$ is modified $1+\alpha$ times. The amplified sub-band $S_{\omega,0}^{'}(x,t)$ can be achieved by the sum of $S_f^{'}(x,t)$. Note that for phase-based motion magnification using octave-bandwidth complex steerable pyramids, the bound for α should satisfy [27] the following:

$$\alpha\delta^s(t) < \frac{\lambda}{4} = \frac{f_s}{4f} \tag{10}$$

where λ is the spatial wavelength corresponding to f captured at a frame rate (or the sampling rate for ultrasonic measurements in this study) of f_s. It can be seen in Eq. (10) that the low-frequency motions could be magnified further than the high-frequency motions. In this study, a larger α is feasible as long as the ultrasonic response s is measured at a higher sampling rate f_s. A higher f_s is much easier to achieve in time-domain signal measurement than in image acquisition.

The above process can be generalized to a 2D sub-band $S_{\omega,0}(x,y,t)$ with local motions $\delta(x,y,t)$ to obtain the amplified sub-band $S_{\omega,0}^{'}(x,y,t)$. The motion-magnified video $I^{'}(x,y,t)$ is then reconstructed by collapsing all the amplified sub-bands $S_{\omega,0}^{'}(x,y,t)$ over all the spatial scales (Eq. (3)).

Step 3: 1D time-domain signal extraction.

The amplified small-motion signal $s_s^{'}$ ($s_s^{'} = s_m^{'} + s_n^{'}$) is extracted from the video $I^{'}(x,y,t)$ using the reverse process in Eq. (5). As shown in Fig. 3, Steps 1–3 are repeated with varying pixel scales Δp until the following condition is satisfied.

$$E_{s_n^{'}} \leq E_{s_n} \tag{11}$$

where $E_{s_n^{'}}$ and E_{s_n} are the noise energies of $s_n^{'}$ and s_n, i.e., the energies of $s_s^{'}$ and s_s minus the components at $f_b \pm f_a$, respectively. The final magnified ultrasonic signal $s^{'}$ is expressed as

$$s^{'} = s_l + s_s^{'} = s_l + s_m^{'} + s_n^{'} \tag{12}$$

where the magnified $s^{'}$ can be used for further nonlinear ultrasonic analysis.

4. Validation with synthetic ultrasonic signals

4.1. Generation of synthetic signals

A group of synthetic ultrasonic signals was generated to evaluate the proposed motion magnification-based nonlinear ultrasonic signal enhancement method. The linear components s_l are unit amplitude sinusoidal signals at $f_a = 45$kHz and $f_b = 206$kHz. The corresponding nonlinear components s_m are at $f_b - f_a = 161$kHz and $f_b + f_a = 251$kHz.

$$s_l = \sin(2\pi f_a t) + \sin(2\pi f_b t) \tag{13}$$

$$s_m = 0.01 \times \sin(2\pi(f_b \pm f_a)t) \tag{14}$$

where the amplitudes of s_m are one hundredth of the amplitudes of s_l.

Synthetic intact s_i and damaged s_d ultrasonic signals were generated with the added Gaussian white noise s_n.

$$s_i = s_l + s_n$$
$$s_d = s_l + s_m + s_n \tag{15}$$

where s_n was created with different signal-to-noise ratios (*SNR* s) with respect to s_m ranging from − 11 to − 47 with a step of − 4. The *SNR* is defined as

$$SNR = 10\log\frac{E_{s_m}}{E_{s_n}}(\text{dB}) \tag{16}$$

where E_{s_m} and E_{s_n} are the energies of s_m and s_n, respectively. The *SNR* was selected such that s_m could be drowned by s_n in the frequency domain as the *SNR* decreased, as shown in Fig. 6. Note that all spectral plots in this study were normalized with respect to its largest linear response. All the s_i and s_d signals were discretely sampled at 1 MHz for 100 ms (100,000 data points). For the motion magnification in this section, each signal was divided into 100 segments ($M = 1000$, $N = 100$), and the magnification factor α was set as two.

4.2. Automated pixel scale selection

Fig. 7(a) shows the noise energy ratio $\frac{E_{s_n}'}{E_{s_n}}$ for an intact signal s_i (*SNR* $= -31$ dB) as the video was constructed with different pixel scales Δp for motion magnification. Fig. 7(b) shows the representative spectral plots of the magnified s_i' corresponding to different Δp. It can be seen that $\frac{E_{s_n}'}{E_{s_n}}$ decreased as Δp increased and the condition in Eq. (11) was satisfied when $\Delta p = 5$. Although Eq. (11) still holds when $\Delta p > 5$, $\Delta p = 5$ was selected because a larger translation $\delta^s(t)$ (proportional to Δp) prevents the selection of a larger magnification factor α, as shown in Eq. (10).

The selected Δp for all the s_i and s_d signals with different *SNR* s are shown in Fig. 8. For s_i, the selected Δp remained constant because the separated small-motion signals s_s only contained noise s_n, and were normalized for video construction (Eq. (5)). However, the selected Δp for s_d varied for different *SNR* s. It was inferred that the signal composition of s_s ($s_s = s_m + s_n$) affected the selection of Δp in the video construction for proper motion magnification.

4.3. Effect of phase denoising

Fig. 9 shows the spectral plots of an intact signal s_i (*SNR* $= -31$ dB) magnified with and without phase denoising. It can be seen that the incorrect motions of noise s_n at $f_b \pm f_a$ could be amplified once phase denoising was omitted from the motion magnification process. Fig. 10 compares the nonlinear modulation parameter β calculated from s_i with various *SNR* s, and the magnified s_i' with and without phase denoising. The β-values remained almost identical between s_i and s_i' with phase denoising (Fig. 10(a)). In contrast, the deviation of the β-values of s_i' without phase denoising from the β-values of s_i progressively increased as the *SNR* decreased (Fig. 10(b)).

4.4. Motion magnification at different orientation

When the time-domain signal was converted into a video, the pixel movement was designated along the x-orientation (Fig. 4). Thereafter, only the sub-bands $S_{\omega,\theta}(x,y,t)$ that decomposed along the x-orientation ($\theta = 0$) were magnified for nonlinear signal enhancement. Fig. 11 shows the spectral plots of the damage signal s_d (*SNR* $= -47$dB) magnified with the sub-bands along the x-orientation ($\theta = 0$) and the y-orientation ($\theta = \frac{\pi}{2}$). It can be seen that the nonlinear components s_m only existed in $S_{\omega,0}(x,y,t)$, and were

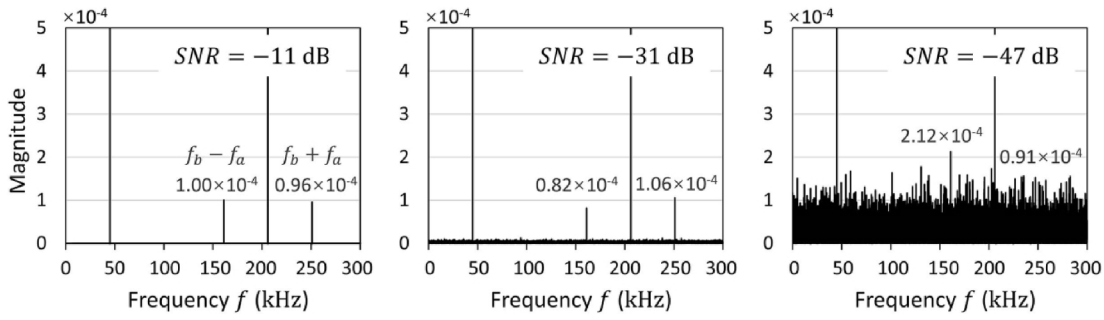

Fig. 6. Representative synthetic signals s_d in the frequency domain when the *SNR* is − 11, −31, and − 47 dB.

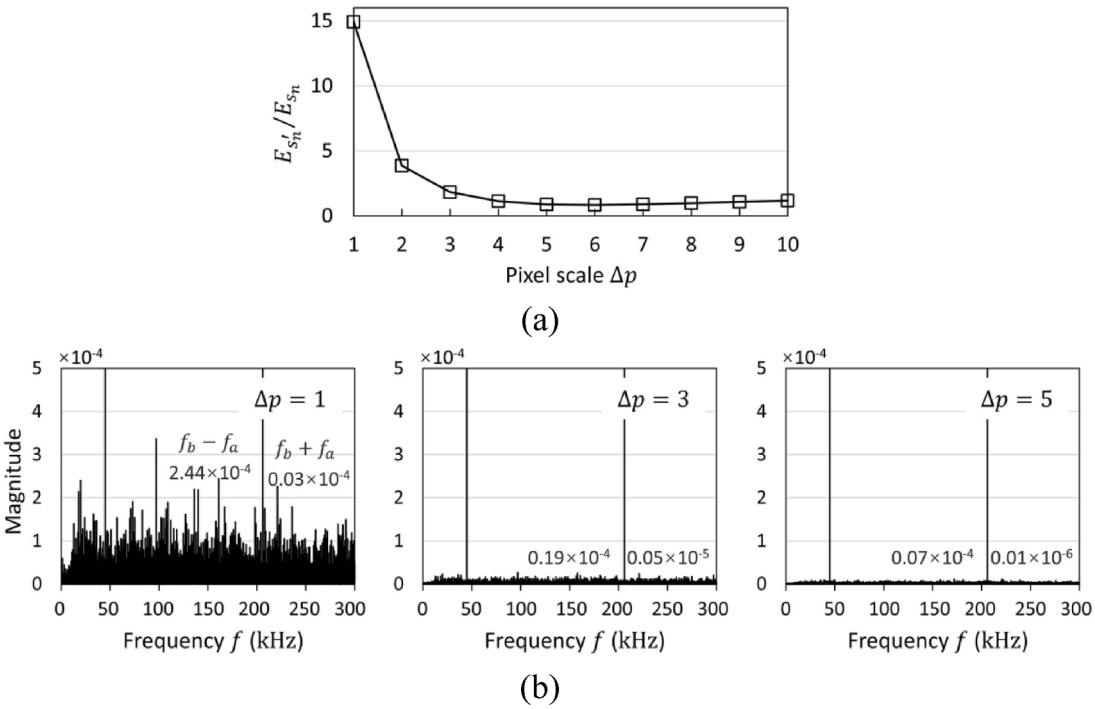

Fig. 7. (a) Noise energy level in the magnified signals of s_i ($SNR = -31$dB) corresponding to different pixel scales. (b) Representative signals magnified at various pixel scales.

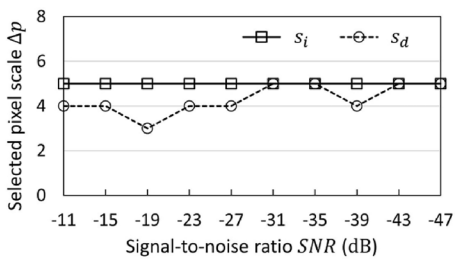

Fig. 8. Pixel scale selection for signals with different *SNR* s.

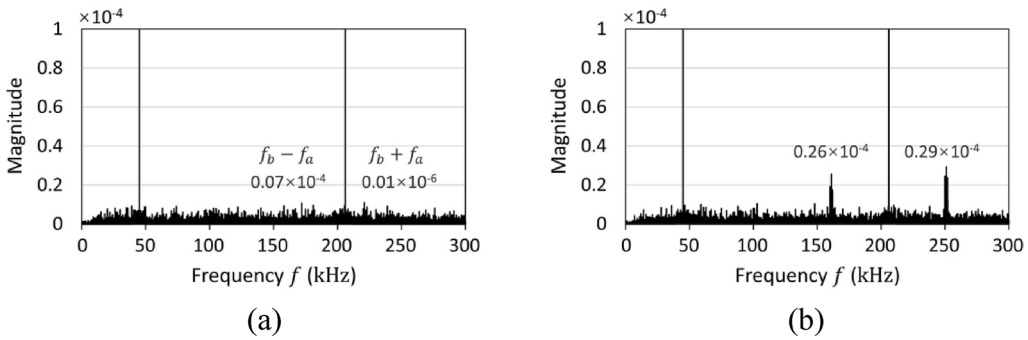

Fig. 9. Representative signal s_i ($SNR = -31$dB) magnified (a) with phase denoising and (b) without phase denoising.

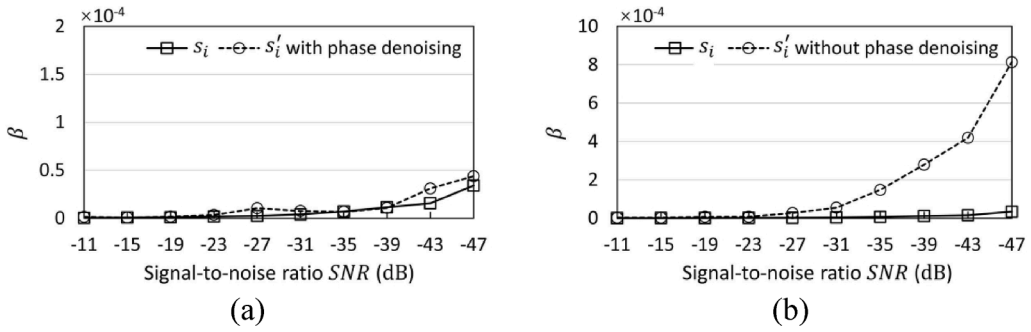

Fig. 10. β of signal s_i with various *SNR* s magnified (a) with phase denoising and (b) without phase denoising.

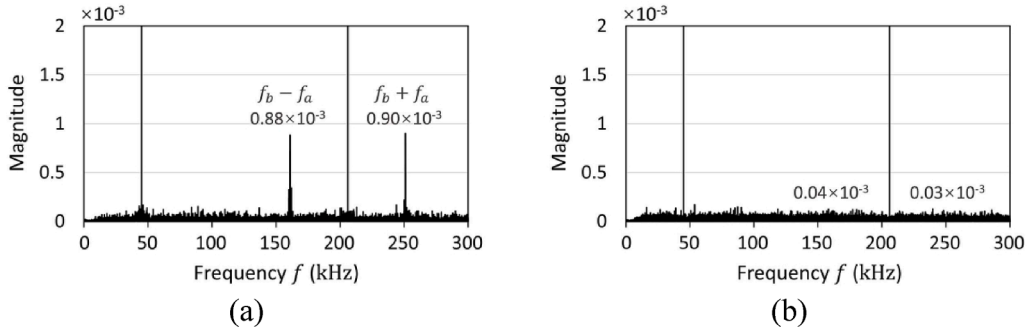

Fig. 11. Representative signal s_d ($SNR = -47$dB) magnified along the (a) *x*-orientation and (b) *y*-orientation.

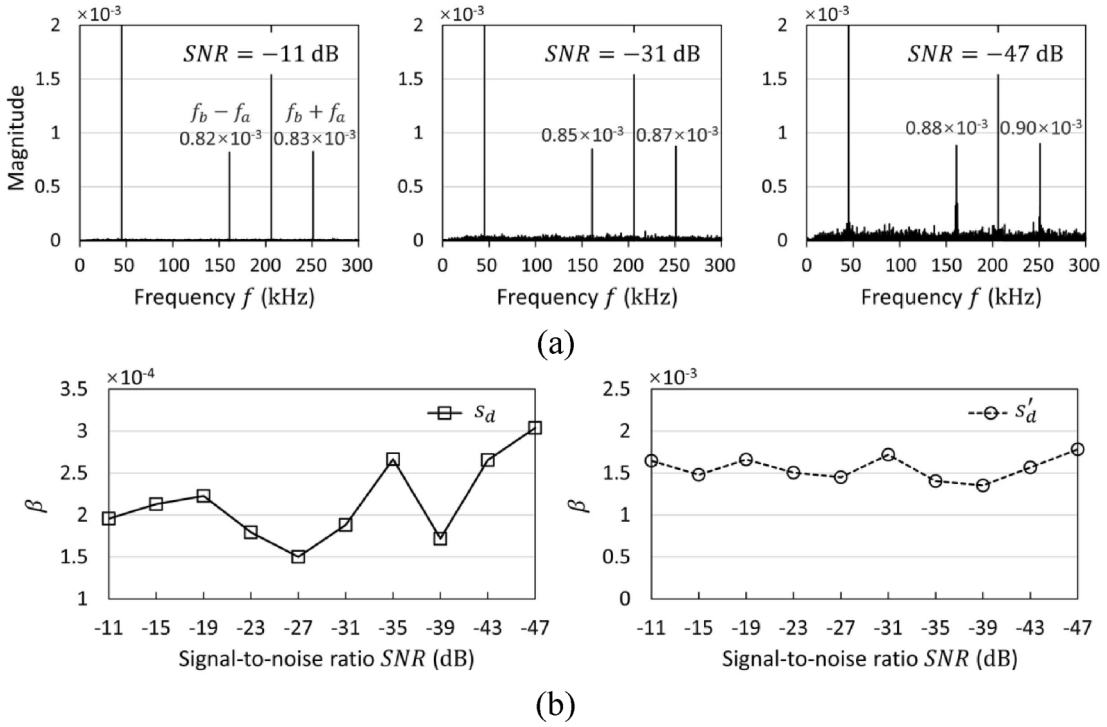

Fig. 12. (a) Representative magnified signals of s_d with different *SNR* s (constant s_m energy). (b) The corresponding β-values of s_d and magnified s_d' signals.

magnified by approximately three times ($=1+\alpha$) (nine times in the spectral plots between Fig. 6 and Fig. 11(a)).

4.5. Validation with various SNRs

Fig. 12(a) shows the representative spectral plots of the magnified signals of s_d with different *SNR* s. The nonlinear components s_m were amplified by approximately the same extent regardless of the noise interference as shown in Fig. 6. Fig. 12(b) shows the β-values of s_d with different *SNR* s and those of the magnified $s_d^{'}$. The relative standard deviation of the β-values of s_d (0.227) was approximately 2.5 times larger than those of the magnified $s_d^{'}$ (0.091).

Another group of damage signals s_d was created with the constant noise s_n but varying amplitudes of the nonlinear components s_m. Here, s_d was expressed as $s_d = s_l + \alpha s_m + s_n$, while the amplitude ratio α of s_m ranged from 0.1 to 1. The noise s_n was obtained at $SNR = -47$dB with respect to s_m. Fig. 13(a) shows the representative spectral plots of the magnified signals of s_d with different amplitude ratios of s_m. Fig. 13(b) shows the β-values of s_d with different amplitude ratios of s_m and those of the magnified $s_d^{'}$. Because the nonlinear components s_m were buried within the noise s_n when the $SNR = -47$dB (Fig. 6), the variations in the amplitude ratio α of s_m had almost no effect on the β-values of s_d (Fig. 13(b)). In contrast, the magnified nonlinear components were clearly observed in $s_d^{'}$ (Fig. 13(a)), and the β-values of $s_d^{'}$ increased proportionally with respect to the amplitude ratio α of s_m (Fig. 13(b)).

5. Application to RFL estimation in a steel padeye

5.1. Experimental procedure

Padeyes are used to connect tension cables in bridges or link an offshore floating structure to its anchorage; hence, they are constantly subjected to cyclic loading and are vulnerable to fatigue failure [33]. In this section, the proposed method was applied to estimate the RFL of a sample padeye made of SM490 steel. As shown in Fig. 14(a), the height and bottom width of the padeye were 132 mm, while the pinhole radius was 22 mm. The thickness of the padeye around the pinhole (including two cheek plates) was 5 mm, while the thickness of the main plate was 3 mm. Three PZTs (APC International, APC850) with a 9 mm diameter and 0.5 mm thickness were attached to the cheek plate for ultrasonic inspection. PZT A and PZT B were used for ultrasonic generation at f_a and f_b, respectively, while PZT C was used for measurement.

As shown in Fig. 14(b), a customized holder was used to fix the padeye to the universal testing machine (UTM, Instron 8801). Cyclic loading at 10 Hz was applied along the y-axis of the sample. The loading amplitudes were 5–50 kN. Fatigue cracks appeared from the edge of the pinhole, and the sample failed at 230 k fatigue cycles (Fig. 14(b)).

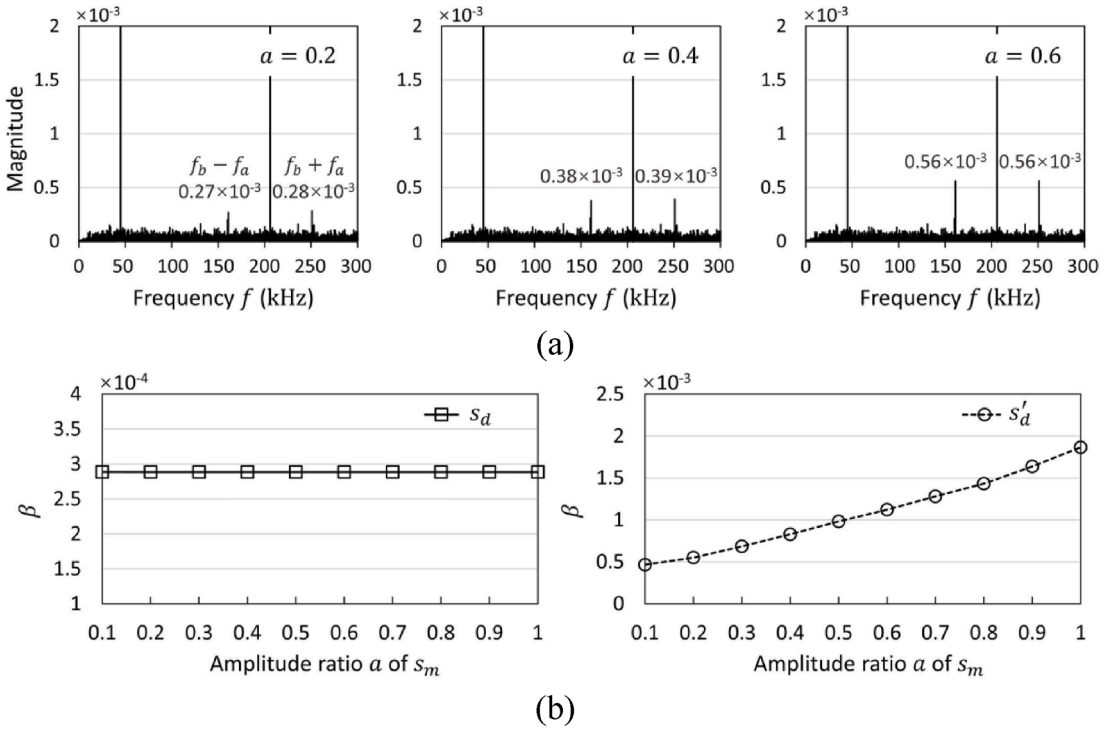

Fig. 13. (a) Representative magnified signals of s_d with different amplitude ratios of s_m (constant s_n energy,$SNR = -47$dB). (b) The corresponding β-values of s_d and magnified $s_d^{'}$ signals.

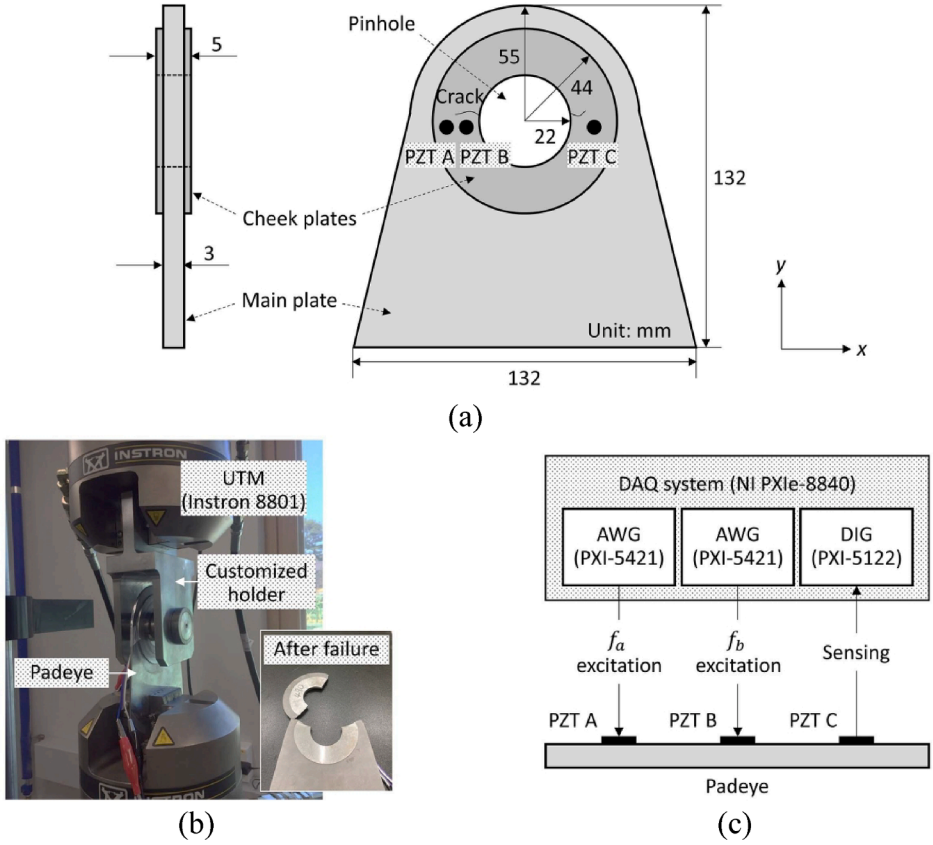

Fig. 14. (a) Steel padeye, (b) fatigue test, and (c) ultrasonic measurement test.

Ultrasonic inspection was periodically performed during the UTM test of the sample. The National Instruments system was adopted for data acquisition, which involved the use of two arbitrary waveform generators (AWG, PXI-5421), a digitizer (DIG, PXI-5122), and a controller (PXIe-8840) (Fig. 14(c)). The input frequencies were selected as $f_a = 50$ kHz and $f_b = 193$ kHz, considering the local resonance characteristics of the sample and to avoid the overlap of $f_b \pm f_a$ with the higher-order harmonic components of f_a [14]. The amplitudes of the two excitations were 12 V. The corresponding ultrasonic response signals s were measured at a 1 MHz sampling rate for 100 ms at different fatigue cycles ($n = 0$, 30, 60, 90, 120, 150, 180, 190, 200, 210, 220 (k)).

5.2. Test results

Fig. 15 shows the ultrasonic response s measured when $n = 30$ k and its magnified s' after motion magnification. Each measured s was divided into 100 segments ($M = 1000$, $N = 100$), while the magnification factor α was set to two. It can be seen in Fig. 15(b) that the nonlinear components at $f_b \pm f_a$ became observable after motion magnification. The nonlinear response at $n = 30$ k was attributed to the inherent material nonlinearity of the padeye sample.

For all the ultrasonic signals measured at different fatigue cycles, the selected pixel scales Δp are shown in Fig. 16. The β-values of s and magnified s' are shown in Fig. 17. Consistent with the previous section, Δp varied as the signal composition (i.e., nonlinear response and noise) changed in the measurements at different fatigue cycles. The β-values in Fig. 17(a) and (b) showed a similar trend as they were calculated before and after motion magnification. When fatigue cracks were initiated during the UTM test, the β-value increased owing to the intensified crack opening and closing. Once the crack length reached the critical value, the fatigue cracks transformed into fracture cracks, and the β-values abruptly decreased [34]. However, the β-values of s (Fig. 17(a)) in the early fatigue cycles (up to 180 k) in the UTM test fluctuated because the weak nonlinear responses caused by material nonlinearity or early stage fatigue cracks could be easily drowned out by the measurement noise.

An RFL estimation method based on nonlinear ultrasonic modulation was adopted [35], which consists of three steps.

First, the appearance of a fatigue crack is detected by observing the increase in the β-values. Once a fatigue crack is detected, it is assumed that crack initiation did not occur until the previous inspection stage (defined as the initial stage). The fatigue cycle at the initial stage is denoted as n_i, and an initial nonlinear parameter β_i is estimated as the β-value at the initial stage. The occurrence of fatigue cracks was detected at 150 k fatigue cycles, as shown in Fig. 17(b); hence, $n_i = 120$ k and $\beta_i = 1.96 \times 10^{-4}$. For the β-values calculated before motion magnification (Fig. 17(a)), owing to their fluctuations in the early phase of the UTM test, it was difficult to

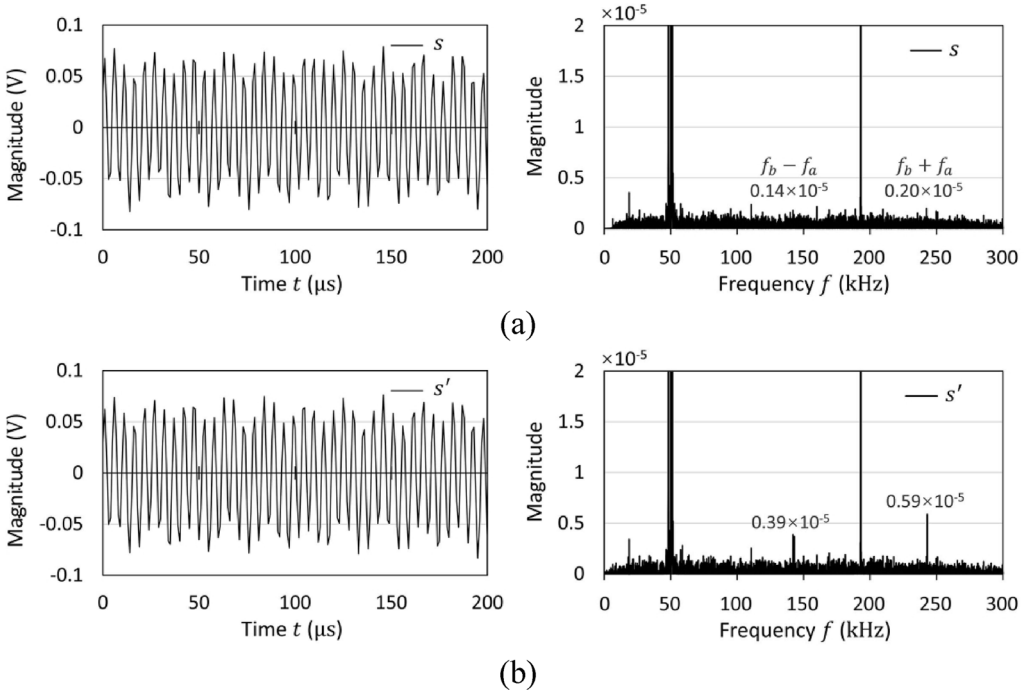

Fig. 15. Representative ultrasonic signals and their spectral plots (a) before motion magnification and (b) after motion magnification (n = 30 k).

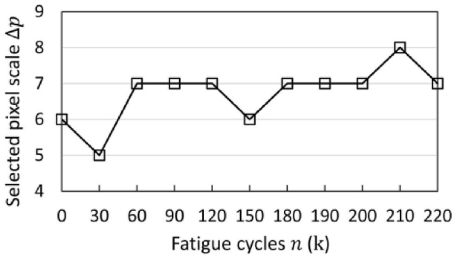

Fig. 16. Pixel scale selection for signals obtained from different fatigue cycles.

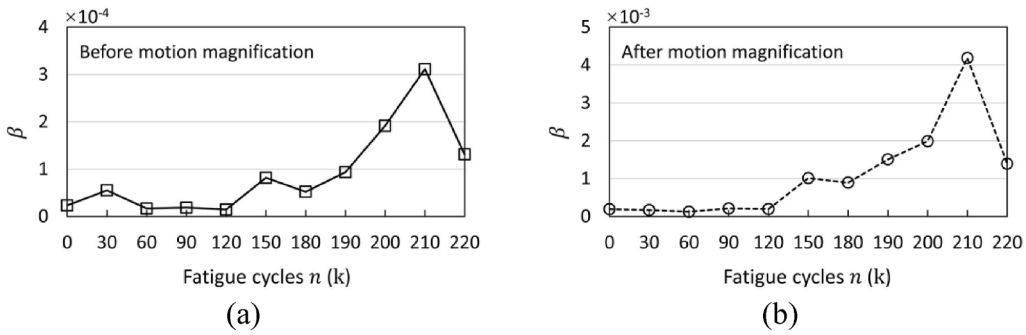

Fig. 17. β-values of the ultrasonic signals calculated (a) before motion magnification and (b) after motion magnification.

identify the emergence of fatigue cracks, which could lead to inaccurate estimates at the initial stage. Here, in this study, the same initial stage (n_i = 120 k) was selected for the RFL estimation using the β-values calculated before motion magnification, and the corresponding $\beta_i = 1.46 \times 10^{-5}$.

Second, a fatigue index (*FI*) is defined as a function of the parameter β to obtain a monotonically increasing relationship between the *FI* and fatigue cycles up to failure.

$$FI(n) = 1 - \left(\frac{\beta_m(n)}{\beta_i}\right)^{-1} \tag{17}$$

where β_m is the maximum β-value up to the current fatigue cycle n, and FI is obtained by normalizing β_m with respect to β_i.

Third, it has been proven that the FI values can be fitted as a power function of the fatigue cycles ($n - n_i$) as

$$FI(n) = A(n - n_i)^B \tag{18}$$

where A and B are estimated by fitting the obtained FI values up to the current fatigue cycles. The total fatigue life of the sample is then acquired as the number of fatigue cycles corresponding to $FI = 1$, thus estimating the RFL.

Fig. 18(a) and (b) show the FI values and fitted power functions obtained at $n = 190$ k and 210 k, respectively. At $n = 190$ k (Fig. 18(a)), the RFLs were estimated as 117.8 k and 67.6 k before and after motion magnification, with corresponding estimation errors of 77.8 k and 27.6 k, respectively. At 210 k (Fig. 18(b)), the RFLs were estimated as 9.1 k and 22 k before and after motion magnification, with lower estimation errors of 10.9 k and 2.0 k, respectively. Table 1 lists the estimated RFLs and estimation errors for four different fatigue cycles. It can be seen that the performance of the RFL estimation model gradually improved as more ultrasonic signals were accumulated during the UTM test. The RFL estimation exhibited better performance using β-values after motion magnification, especially at the early stage of the UTM test. This confirms that the proposed method effectively enhanced the nonlinear components and resisted noise interference even when the nonlinear components were buried in the noise.

A long short-term memory (LSTM) network for noise reduction was adopted for comparison [25]. An LSTM network is trained to learn the inherent sequential patterns from ultrasonic measurements, including the nonlinear responses, and it does not require any pre-knowledge of the nonlinear frequencies. Here, a prediction of 100 ms (same as the signal length used for motion magnification) with reduced noise was obtained from the trained LSTM network and used for β calculation. Fig. 19(a) shows the spectral plot of the predicted signal at $n = 30$ k. It can be seen that the noise was effectively reduced compared with the original signal in Fig. 15(a). However, the weak nonlinear components due to inherent material nonlinearity were hardly observed compared with the result after motion magnification (Fig. 15(b)). Fig. 19(b) shows the β-values calculated using the predicted signals at different fatigue cycles. A similar trend was observed in Fig. 17, but the amplitudes of β were similar to those in Fig. 17(a) before motion magnification. This is because the LSTM network focused on noise suppression rather than nonlinear signal enhancement. Table 2 lists the estimated RFLs at different fatigue cycles based on the β-values in Fig. 19(b). The accuracy improvement of the estimated RFLs was not as high as that in Table 1 with motion magnification, given that the proposed method actively enhanced the nonlinear modulations and suppressed noise.

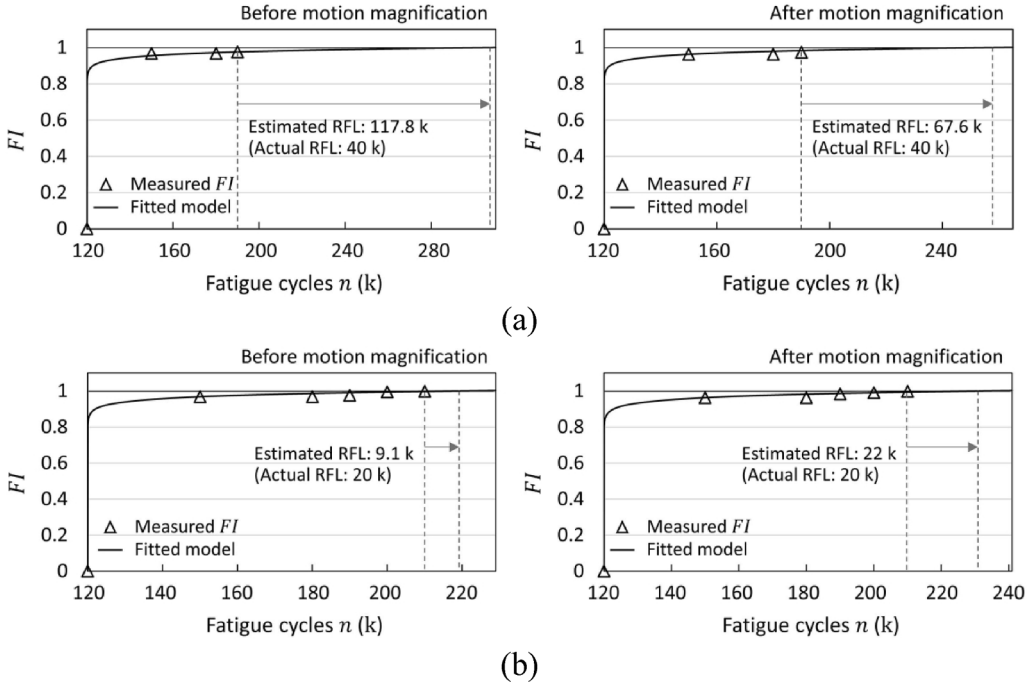

Fig. 18. RFL estimation results before/after motion magnification at (a) $n = 190$k and (b) $n = 210$k.

Table 1
RFL estimation results at different fatigue cycles.

	Current cycles	Estimated RFL	Error
Before motion magnification	190 k	117.8 k	77.8 k
	200 k	85.0 k	55.0 k
	210 k	9.1 k	10.9 k
	220 k	9.1 k	0.9 k
After motion magnification	190 k	67.6 k	27.6 k
	200 k	54.0 k	24.0 k
	210 k	22.0 k	2.0 k
	220 k	9.3 k	0.7 k

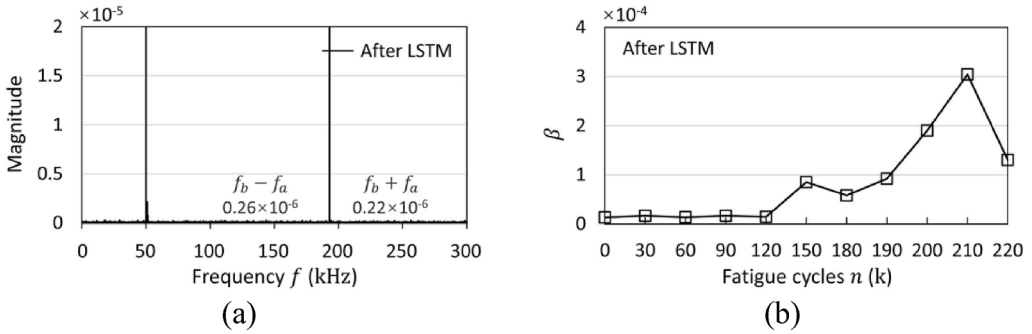

Fig. 19. (a) Representative ultrasonic signal predicted by the LSTM network ($n = 30$ k). (b) The corresponding β-values of the predicted ultrasonic signals at different fatigue cycles.

Table 2
RFL estimation results with the LSTM network.

	Current cycles	Estimated RFL	Error
With LSTM network	190 k	119.6 k	79.6 k
	200 k	58.5 k	28.5 k
	210 k	9.1 k	10.9 k
	220 k	9.3 k	0.7 k

6. Conclusion

In this study, a motion magnification-based nonlinear ultrasonic signal enhancement method was proposed. A 2D video was first constructed from a 1D time-domain ultrasonic signal with an automatically selected pixel scale. Then, the constructed 2D video was spatially decomposed into multiple sub-bands with different scales. The subtle motions of the nonlinear responses of interest were amplified by temporally filtering and modifying the phase variations in each sub-band. The magnified 2D video was reconstructed by collapsing all the amplified sub-bands, from which a magnified ultrasonic signal could be extracted for further nonlinear ultrasonic analysis. Based on the validation tests with the synthetic and experimental data shown in this study, the following conclusions can be drawn:

(1) Because a 1D time-domain signal was used to establish the pixel movements in a 2D video with a predefined moving orientation, only the decomposed sub-bands along the same moving orientation required processing ($\theta = 0$ in this study).
(2) The sub-bands decomposed at various spatial scales with complex steerable pyramids helped capture the subtle motions of the nonlinear responses even when they were buried in noise ($SNR = -47$dB in this study). Noise was further suppressed by spatially low-pass filtering the phase variations in the decomposed sub-bands.
(3) The small-motion signal that contained nonlinear components was easily separated from the ultrasonic measurement with known input frequencies, and temporal filtering was readily designed as a bandpass of the modulation frequencies. Temporal filtering can be modified to enhance different nonlinear components (e.g., harmonics or higher-order modulations).
(4) A more accurate RFL estimate at the early stage of fatigue life could be obtained with the proposed nonlinear ultrasonic signal enhancement method than with the conventional signal analysis method.

The limitations of the proposed method include high computational costs, especially that for phase denoising, and the requirement of a sufficiently long time-domain signal (100 ms in this study). Future work is warranted to investigate different strategies to convert a

time-domain signal into a 2D video, increase the magnification factor ($\alpha = 2$ in this study), and explore applications in noisy environments, such as ultrasonic inspection in metal additive manufacturing.

Declaration of Competing Interest

The authors declare that they have no known competing financial interests or personal relationships that could have appeared to influence the work reported in this paper.

Data availability

Data will be made available on request.

Acknowledgements

This work was supported by a National Research Foundation of Korea (NRF) grant funded by the Korean government (MSIT) [Grant number 2019R1A3B3067987].

References

[1] J.H. Cantrell, W.T. Yost, Nonlinear ultrasonic characterization of fatigue microstructures, Int. J. Fatigue 23 (2001) 487–490.
[2] V. Marcantonio, D. Monarca, A. Colantoni, M. Cecchini, Ultrasonic waves for materials evaluation in fatigue, thermal and corrosion damage: a review, Mech. Syst. Sig. Process. 120 (2019) 32–42.
[3] C.J. Lissenden, Nonlinear ultrasonic guided waves—principles for nondestructive evaluation, J. Appl. Phys. 129 (2021), 021101.
[4] K.-Y. Jhang, Nonlinear ultrasonic techniques for nondestructive assessment of micro damage in material: a review, Int. J. Precis. Eng. Manuf. 10 (1) (2009) 123–135.
[5] C. Andreades, G.P.M. Fierro, M. Meo, A nonlinear ultrasonic modulation approach for the detection and localisation of contact defects, Mech. Syst. Sig. Process. 162 (2022), 108088.
[6] I. Jeon, H.J. Lim, P. Liu, B. Park, A. Heinze, H. Sohn, Fatigue crack detection in rotating steel shafts using noncontact ultrasonic modulation measurements, Eng. Struct. 196 (2019), 109293.
[7] S. Mezil, N. Chigarev, V. Tournat, V. Gusev, Evaluation of crack parameters by a nonlinear frequency-mixing laser ultrasonics method, Ultrasonics 69 (2016) 225–235.
[8] P. Liu, J. Jang, H. Sohn, Crack localization by laser-induced narrowband ultrasound and nonlinear ultrasonic modulation, Smart Struct. Syst. An Int. J. 25 (2020) 301–310.
[9] X. Qin, C. Peng, G. Zhao, Z. Ju, S. Lv, M. Jiang, Q. Sui, L. Jia, Full life-cycle monitoring and earlier warning for bolt joint loosening using modified vibro-acoustic modulation, Mech. Syst. Sig. Process. 162 (2022), 108054.
[10] X. Chen, J.-Y. Kim, K. Kurtis, J. Qu, C. Shen, L. Jacobs, Characterization of progressive microcracking in Portland cement mortar using nonlinear ultrasonics, NDT and E Int. 41 (2008) 112–118.
[11] B. Boll, E. Willmann, B. Fiedler, R.H. Meißner, Weak adhesion detection–enhancing the analysis of vibroacoustic modulation by machine learning, Compos. Struct. 273 (2021), 114233.
[12] Z. Prevorovsky, J. Krofta, J. Kober, M. Chlada, A. Kirchner, Non-linear ultrasonic spectroscopy of 3D printed metallic samples, Insight-Non-Destruct. Test. Condition Monitor. 61 (2019) 157–161.
[13] P. Liu, K. Yi, Y. Park, H. Sohn, Ultrafast nonlinear ultrasonic measurement using femtosecond laser and modified lock-in detection, Opt. Lasers Eng. 150 (2022), 106844.
[14] H. Lim, H. Sohn, P. Liu, Binding conditions for nonlinear ultrasonic generation unifying wave propagation and vibration, Appl. Phys. Lett. 104 (2014), 214103.
[15] K. Dziedziech, L. Pieczonka, M. Adamczyk, A. Klepka, W.J. Staszewski, Efficient swept sine chirp excitation in the non-linear vibro-acoustic wave modulation technique used for damage detection, Struct. Health Monit. 17 (2018) 565–576.
[16] P. Liu, H. Sohn, T. Kundu, S. Yang, Noncontact detection of fatigue cracks by laser nonlinear wave modulation spectroscopy (LNWMS), NDT and E Int. 66 (2014) 106–116.
[17] T. Kundu, J.N. Eiras, W. Li, P. Liu, H. Sohn, J. Payá, Fundamentals of nonlinear acoustical techniques and sideband peak count, in: T. Kundu (Ed.), Nonlinear Ultrasonic and Vibro-Acoustical Techniques for Nondestructive Evaluation, Springer International Publishing, Cham, 2019, pp. 1–88.
[18] P. Liu, H. Sohn, S. Yang, T. Kundu, Fatigue crack localization using noncontact laser ultrasonics and state space attractors, J. Acoust. Soc. Am. 138 (2015) 890–898.
[19] Y. He, K. Wang, L. Xu, H. Sohn, Z. Su, Laser ultrasonic imaging of submillimeter defect in a thick waveguide using entropy-polarized bilateral filtering and minimum variance beamforming, Mech. Syst. Sig. Process. 186 (2023), 109863.
[20] N. Li, J. Sun, J. Jiao, B. Wu, C. He, Quantitative evaluation of micro-cracks using nonlinear ultrasonic modulation method, NDT and E Int. 79 (2016) 63–72.
[21] A.J. Hillis, S.A. Neild, B.W. Drinkwater, P.D. Wilcox, Global crack detection using bispectral analysis, Proc. Royal Soc. A: Math. Phys. Eng. Sci. 462 (2006) 1515–1530.
[22] J. Wang, Y. Shen, D. Rao, W. Xu, An instantaneous-baseline multi-indicial nonlinear ultrasonic resonance spectral correlation technique for fatigue crack detection and quantification, Nonlinear Dyn. 103 (2021) 677–698.
[23] P. Liu, H. Sohn, Development of nonlinear spectral correlation between ultrasonic modulation components, NDT and E Int. 91 (2017) 120–128.
[24] W. Xu, X. Li, J. Zhang, Z. Xue, J. Cao, Ultrasonic signal enhancement for coarse grain materials by machine learning analysis, Ultrasonics 117 (2021), 106550.
[25] J. Jang, H. Sohn, H.J. Lim, Spectral noise and data reduction using a long short-term memory network for nonlinear ultrasonic modulation-based fatigue crack detection, Ultrasonics 129 (2023), 106909.
[26] C. Liu, A. Torralba, W.T. Freeman, F. Durand, E.H. Adelson, Motion magnification, ACM Trans. Graphics (TOG) 24 (2005) 519–526.
[27] N. Wadhwa, M. Rubinstein, F. Durand, W.T. Freeman, Phase-based video motion processing, ACM Trans. Graphics (TOG) 32 (2013) 1–10.
[28] T.-H. Oh, R. Jaroensri, C. Kim, M. Elgharib, F.e. Durand, W.T. Freeman, W. Matusik, Learning-based video motion magnification, in: Proceedings of the European Conference on Computer Vision (ECCV), 2018, pp. 633-648.
[29] E. Cai, Y. Zhang, S.T. Quek, Visualizing and quantifying small and nonstationary structural motions in video measurement, Comput. Aided Civ. Inf. Eng. 38 (2023) 135–159.
[30] Q. Qiu, D. Lau, Defect detection in FRP-bonded structural system via phase-based motion magnification technique, Struct. Control Health Monit. 25 (12) (2018) e2259.
[31] M. Eitner, B. Miller, J. Sirohi, C. Tinney, Effect of broad-band phase-based motion magnification on modal parameter estimation, Mech. Syst. Sig. Process. 146 (2021), 106995.
[32] E. Cai, Y. Zhang, Gaussian mixture model based phase prior learning for video motion estimation, Mech. Syst. Sig. Process. 175 (2022), 109103.

[33] S. Boljanović, S. Maksimović, Fatigue crack growth modeling of attachment lugs, Int. J. Fatigue 58 (2014) 66–74.
[34] J. Cheng, J.N. Potter, A.J. Croxford, B.W. Drinkwater, Monitoring fatigue crack growth using nonlinear ultrasonic phased array imaging, Smart Mater. Struct. 26 (2017), 055006.
[35] H.J. Lim, H. Sohn, Online fatigue crack prognosis using nonlinear ultrasonic modulation, Struct. Health Monit. 18 (2019) 1889–1902.